SCIENTIFIC REPORTS

OPEN

SUBJECT AREAS:
MATERIALS FOR ENERGY AND CATALYSIS
BATTERIES

Received
29 November 2013

Accepted
20 March 2014

Published
15 April 2014

Correspondence and requests for materials should be addressed to C.S.O. (cozkan@engr.ucr.edu) or M.O. (mihri@ee.ucr.edu)

Stable Cycling of SiO_2 Nanotubes as High-Performance Anodes for Lithium-Ion Batteries

Zachary Favors[1], Wei Wang[1,2], Hamed Hosseini Bay[1], Aaron George[1], Mihrimah Ozkan[2] & Cengiz S. Ozkan[1]

[1]Materials Science and Engineering Program, Department of Mechanical Engineering, University of California Riverside, CA 92521 (USA), [2]Department of Electrical Engineering, Department of Chemistry, University of California, University of California Riverside, CA 92521 (USA).

Herein, SiO_2 nanotubes have been fabricated via a facile two step hard-template growth method and evaluated as an anode for Li-ion batteries. SiO_2 nanotubes exhibit a highly stable reversible capacity of 1266 $mAhg^{-1}$ after 100 cycles with negligible capacity fading. SiO_2 NT anodes experience a capacity increase throughout the first 80 cycles through Si phase growth via SiO_2 reduction. The hollow morphology of the SiO_2 nanotubes accommodates the large volume expansion experienced by Si-based anodes during lithiation and promotes preservation of the solid electrolyte interphase layer. The thin walls of the SiO_2 nanotubes allow for effective reduction in Li-ion diffusion path distance and, thus, afford a favorable rate cyclability. The high aspect ratio character of these nanotubes allow for a relatively scalable fabrication method of nanoscale SiO_2-based anodes.

Silicon, as an anode material, has been extensively researched in recent years due to its high theoretical capacity of 3579 $mAhg^{-1}$ and relative abundance[1,2]. However, Si undergoes volume expansion upwards of 300% upon lithiation generating large mechanical stresses and subsequent pulverization and solid electrolyte interphase (SEI) degradation[3,4]. Effective structuring of Si below a critical dimension of 150 nm via nanospheres, nanoparticles, nanotubes, and nanowires has alleviated pulverization and subsequent active material loss associated with the lithiation induced volume expansion[5–9]. Even fewer structures have addressed the crucial stability of the SEI layer such as double walled silicon nanotubes, highly porous silicon nanowires, and yolk-shell silicon nanoparticles[10–12]. However, many of these exotic structures lack scalability such as those fabricated via chemical vapor deposition (CVD) using silane: an expensive, toxic, and pyrophoric precursor[12,13]. Attention has recently turned to SiO_2 as a viable anode material for Li-ion batteries due to its high abundance in the earth's crust, low discharge potential, and high initial irreversible capacity and reversible capacity of 3744 $mAhg^{-1}$ and 1961 $mAhg^{-1}$, respectively[14–16]. Myriad SiO_2-based architectures have been fabricated and characterized as anodes including nanocubes, tree-like thin films, and carbon coated nanoparticles[17–19]. Non-stoichiometric silicon oxides (SiO_x, where $0 < x < 2$) have also attracted attention due the higher molar ratio of silicon to oxygen[20,21]. A lower oxygen content allows for higher specific capacity at the expense of cyclability[22].

Numerous other material systems have been investigated as anodes for Li-ion batteries. Carbon-based anodes such as graphite, 3D graphene sheets, carbon nanotubes (CNTs), and CNT pillared graphene have all been demonstrated as feasible material systems for lithium-ion batteries[23–26]. Many of these carbon nanostructures can also be used as high-performance supercapacitor materials, such as chrysanthemum like carbon nanofibers, 3D graphene and CNT foam, and functionalized graphene sheets[27–30]. While the rate capability of carbon-based anodes is superior to that of silicon-based anodes, the specific capacity is inferior to that of silicon-based anodes. Graphite, typically used in commercial Li-ion battery anodes, has a theoretical capacity of 372 $mAhg^{-1}$, which is not sufficient for next generation Li-ion batteries[31]. Tin, with a theoretical capacity of 972 $mAhg^{-1}$, has also garnered interest as a possible anode material with structures such as encapsulated Sn nanoparticles and Sn nanowires[32,33]. However, Sn experiences similar lithiation-induced expansion issues like Si and has a lower specific capacity.

Polydimethylsiloxane (PDMS) is an optically transparent, non-toxic, and environmentally benign organosilicon widely used in pharmaceutical and consumer applications[34,35]. PDMS produces SiO_2 vapor species when

heated in ambient atmosphere, which makes it an ideal precursor for templated deposition of SiO_2 at the nanoscale. Beginning at 290°C, PDMS will thermally degrade into volatile cyclic oligomers via chain-folded scission of Si-O bonds by oxygen-catalyzed depolymerization[36,37]. The ability for PDMS to produce SiO_2 vapor allows for deposition of SiO_2 on a variety of templates. Specifically, hollow nanostructures are of interest for Li-ion batteries due to reduced Li-ion diffusion path distance via increased surface area and small wall thicknesses[38,39]. Alleviation of lithiation-induced mechanical stresses can also be accomplished through engineering interior voids in the active material[40,41]. Herein, we present a modified procedure for fabricating high aspect ratio SiO_2 NTs, previously presented by Hu et al., and evaluate their performance as Li-ion battery anodes[42].

Results

The fabrication process for silicon sub-oxide nanotubes (SiO_2 NTs) is illustrated schematically in Fig. 1. An amorphous layer of SiO_2 is deposited onto commercial AAO templates via vapor phase deposition through thermal degradation of PDMS in air under vacuum. Our improved synthesis procedure eliminates the need to sand excess SiO_2 deposits off of the fragile AAO templates after deposition. By placing the AAO templates downstream from, rather than covering, the PDMS blocks and performing the deposition process under vacuum, we are better able to control SiO_2 deposition throughout the AAO template, preventing unwanted thick deposits of SiO_2. SiO_2 conformally coats all exposed surfaces of the AAO including the top and bottom of the template, creating a connected tubular network of SiO_2. The AAO is subsequently removed via a heated phosphoric acid bath to leave SiO_2 NTs. After rinsing several times in DI water to remove phosphoric acid, the tubes are sonicated to separate the bundles of SiO_2 NTs into individual tubes. The connected SiO_2 NT network obtained after AAO removal is not mechanically sound, therefore the tubes must be sonicated apart so that they may be handled facilely in powder form. A 20 nm coating of SiO_2 on a 13 mm diameter AAO with a thickness of 50 μm produces a volumetric density of SiO2 of 0.515 gcm^{-3} and an areal density of 2.57 $mgcm^{-2}$.

SEM images in Fig. 2 reveal the tubular morphology of the SiO_2 NTs as well as their high aspect ratio. Bundles of SiO_2 NTs occur due to deposition of SiO_2 on the tops and bottoms of the AAO templates, but brief sonication serves to easily liberate the tubes. The SEM image in Fig. 2(a) reveals the excellent uniformity of the SiO_2 coating across all dimensions of the AAO templates and the interconnected nature of the SiO_2 NTs after removal of the AAO template. These small bundles occur after a brief period of sonication and further sonication serves to fully separate all of the tubes, as seen in Fig. 2(b). The tubes have a very high aspect ratio of 250 : 1 at a length of 50 μm and an average diameter of 200 nm. Lengthy periods of sonication fully separate and shorten the SiO_2 NTs, revealing their tubular morphology as seen in Fig. 2(c). The SEM image in Fig. 2(d) reveals the branched morphology of the SiO_2 NTs, which serves to further increase the surface area of the tubes and is purely a result of anodization in the presence of aluminum imperfections[43].

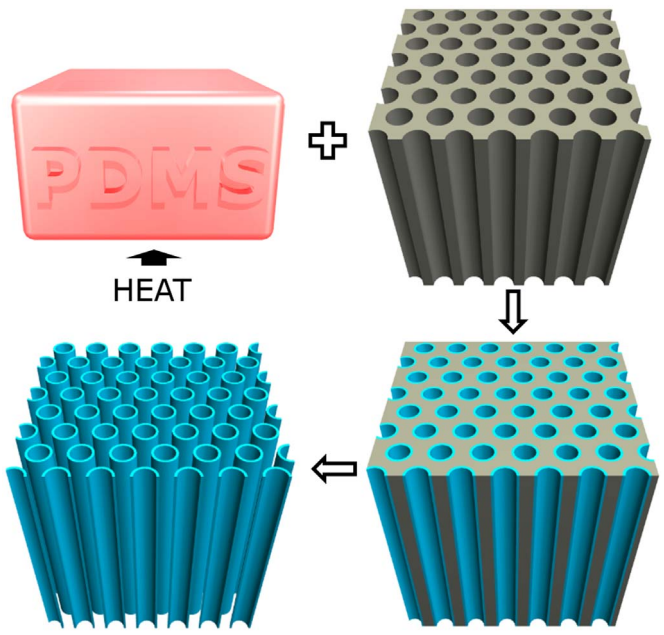

Figure 1 | Schematic representation of the fabrication process for SiO_2 NTs.

TEM images reveal the wall thickness is 20 nm and highly uniform throughout the length of the tubes as in Fig. 2(e). The branched nature of the NTs is confirmed via TEM and no evidence suggests porosity exists in the walls. TEM confirms the SiO_2 NTs have an average diameter of 200 nm, which is expected given the commercial AAO template specifications. Based on the highly random fracture patterns generated via sonication, we conclude that the tubes are composed of amorphous SiO_2. XRD analysis confirms that the SiO_2 NTs are amorphous as seen in Fig. 2(f). Regardless of initial crystallinity, SiO_2 NTs will undoubtedly be amorphous in subsequent cycles[44,45].

Scanning transmission electron microscopy (STEM) and energy dispersive spectroscopy (EDS) are further performed to confirm the composition of the as-prepared nanotube samples. The STEM-EDS sample was simply prepared via transferring vacuum-dried SiO_2 NTs onto a copper TEM grid. As shown in Figure 3a, SiO_2 NTs are randomly oriented, and a selected area EDS mapping was performed on the region within the yellow box. EDS microanalysis on the selected region shows the SiO_2 NTs consists of primarily Si and O (Figure 3b). EDS element mapping micrographs of Si and O suggest a very uniform distribution of these two elements. Traceable amount of C, Al, P (wt% $< 1\%$) were observed due to carbon contaminates, unetched AAO, and unremoved H_3PO_4 etchant, respectively. An EDS quantitative analysis on the selected region was performed to characterize the weight and atomic percentages of elements and to confirm the existence of SiO_2, as in Fig. 3 e–f. We believe the contaminants and the copper grid both contribute to the oxygen peak due to the existence of respective oxides from each.

The Langmuir and BET surface areas were measured to be 45.17 and 26.64 m^2g^{-1}, respectively, for the as-prepared SiO_2 NTs. The obtained surface area and pore distribution suggest the as-prepared SiO_2 NTs have limited surface area and porosity as in Fig. 4. This surface area is more than double the surface area of as-received AAO templates which is expected given the tubular morphology[46]. This limited surface area is beneficial in reducing the amount of SEI layer formation in the first few cycles by limiting active material contact with the electrolyte[47]. However, the rate capability suffers as a result of the limited surface area due to a higher reliance on bulk diffusion of Li into SiO_2.

The electrochemical performance of SiO_2 NTs was characterized by fabricating 2032 coin cells with SiO_2 anodes and Li metal counter electrodes. Cyclic voltammetry (CV) was performed in the 0–3.0 V range with a scan rate of 0.1 mVs^{-1}, shown in Fig. 4(a). The CV plot is shown to 1.75 V to emphasize the noteworthy reactions taking place at lower voltages. Decomposition of the electrolyte and formation of the SEI layer occurs at the broad peak of 0.43 V as in Fig. 5(a). A much broader, less discernable peak occurs at 1.40 V which can be attributed to a reaction between electrolyte and electrode and the beginning of SEI formation[48]. Both of these peaks become undiscernible in the 2nd cycle suggesting SEI formation takes place mostly during the first cycle and that these initial reactions are irreversible. During the initial charge cycle a noticeable peak occurs at 0.33 V, which can be attributed to dealloying. In subsequent cycles this peak

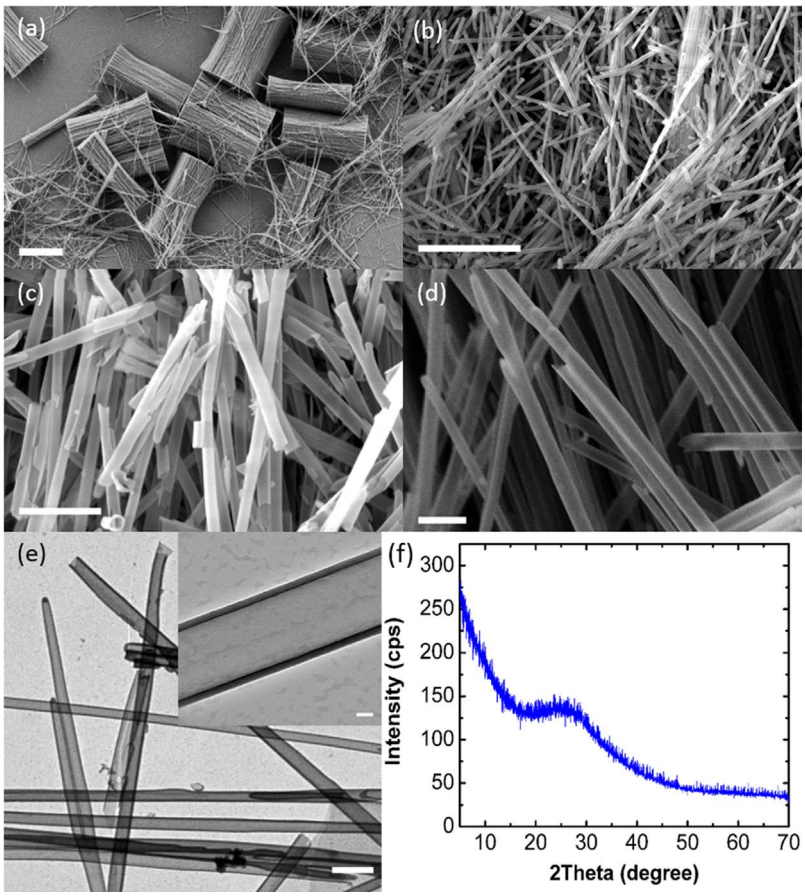

Figure 2 | SEM image of (a) partially separated SiO_2 NTs showing NT bundles and dispersed NTs, (b) fully separated dispersed SiO_2 NTs, (c) separated SiO_2 NTs showing tubular morphology, and (d) image showing branched morphology. Scale bars are 25 μm, 10 μm, 2 μm, and 1 μm for (a), (b), (c), and (d), respectively. (e) TEM image of dispersed SiO_2 NTs and inset showing tube diameter and wall thickness. Scale bar is 400 nm and 50 nm for the inset. (f) XRD analysis of SiO_2 NTs.

becomes very pronounced and shifts downward to 0.25 V. The sharpening and growth of this dealloying peak implies a rate enhancement in the kinetic process of delithiation of SiO_2 NTs. The kinetic enhancement may be due to the formation of an embedded nano-Si phase as it has been reported that one of the oxidation peaks of Si is 0.25 V during Li extraction from Li_xSi[49]. By the 10th cycle there is an emergence of an anodic peak located at 0.22 V while the peak at 0.01 V has decreased. It is known in the literature that the 0.01 V and 0.22 V peaks are associated with the lithiation of Si[48,50]. The CV curves are in good agreement with the charge-discharge profiles in Fig. 5(c) and Fig. 5(d).

Galvanostatic cycling of SiO_2 NTs using a C rate of 100 mAg^{-1} was performed for 100 cycles at selected current densities. The initial sharp decrease in charge capacity over the first few cycles, seen in Fig 5(b), can be attributed to the formation of the SEI layer. The very thin walls of the SiO_2 NTs allows for lithiation of a larger percentage of active material and thus the marked high capacity relative to other published SiO_2 anodes utilizing thicker structures[20,51]. The initial charge capacity is 2404 $mAhg^{-1}$ using a rate of C/2, and the initial discharge capacity is 1040 $mAhg^{-1}$ yielding a 1st cycle efficiency of 43.3%; this is attributed to the SEI formation. After 10 cycles the charge capacity levels off to 1101 $mAhg^{-1}$ and the discharge capacity increases to 1055 $mAhg^{-1}$; this yields an efficiency of 95.8%. Expectedly, cycling at higher rates produces lower charge capacities as follows: 1008 $mAhg^{-1}$ at 1C, 914 $mAhg^{-1}$ at 2C, and 814 $mAhg^{-1}$ at 4C. After 100 cycles the charge and discharge capacity increase to 1266 $mAhg^{-1}$ and 1247 $mAhg^{-1}$, respectively; the efficiency is 98.5%.

Discussion

Yan et al. confirmed a coexistence of the irreversible lithiation mechanisms in reaction 1a and 1b[19,21]. The electrochemically inactive and thermodynamically stable compounds in reaction 1 and 2 are also responsible for the low efficiency in the first charge-discharge cycle, but they may form a stable scaffolding that alleviates volume expansion related issues associated with lithiation of Si[52]. This inactive lithium silicate scaffolding coupled with the tubular morphology of the SiO_2 NTs may be responsible for the highly stable cycling and low capacity fading. As the silicon phase grows larger, volume expansion effects become more significant and lead to capacity fading as seen in other Si and SiO_2 anodes[18,53]. The losses associated with expansion related effects such as SEI degradation and active material pulverization begin to outweigh gains in capacity from Si phase growth. Reaction 1c is responsible for the reversible capacity as seen in traditional Si-based anodes resulting in the formation of $Li_{15}Si_4$ at room temperature[5].

$$SiO_x + yLi + ye \rightarrow Si + Li_yO_x \quad (1a)$$

$$yLi + SiO_x \rightarrow Li_ySiO_x \quad (1b)$$

$$Li + Si + xe \leftrightarrow Li_xSi \quad (1c)$$

After the initial decrease in capacity due to SEI formation, the capacity steadily increases until stabilizing at around 80 cycles. We believe this capacity increase is due to the increasing amount of silicon as the SiO_2 is partially reduced by Li and not fully reduced back to SiO_2. Ban

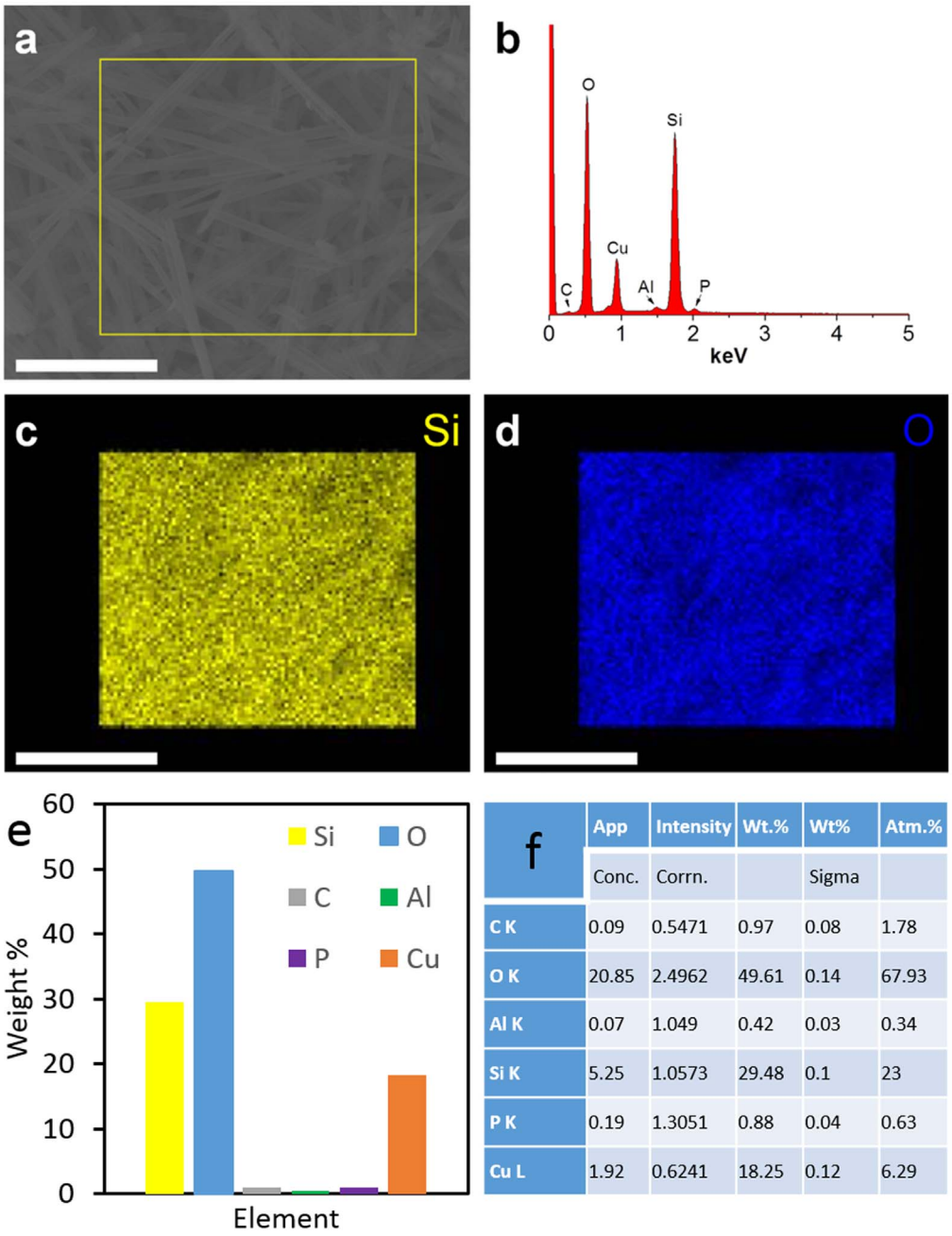

f	App	Intensity	Wt.%	Wt%	Atm.%
	Conc.	Corrn.		Sigma	
C K	0.09	0.5471	0.97	0.08	1.78
O K	20.85	2.4962	49.61	0.14	67.93
Al K	0.07	1.049	0.42	0.03	0.34
Si K	5.25	1.0573	29.48	0.1	23
P K	0.19	1.3051	0.88	0.04	0.63
Cu L	1.92	0.6241	18.25	0.12	6.29

Figure 3 | (a) SEM image of SiO_2 NTs. (b) EDS spectra of SiO_2 NTs on selected region (yellow rectangle) of image a. (c–d) show the EDS microanalysis of element Si and O for this selected region. Scale bar: 5 μm. (e–f) EDS quantitative analysis of selected region.

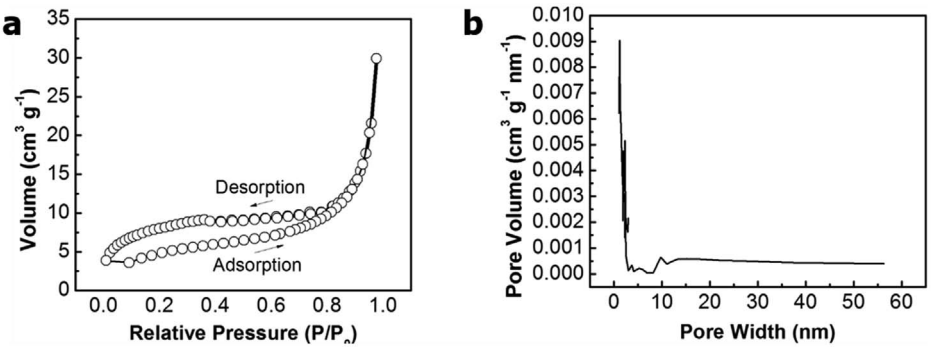

Figure 4 | (a) Type IV N_2 adsorption and desorption isotherms for SiO_2 NTs. (b) Pore size distribution of SiO_2 NTs.

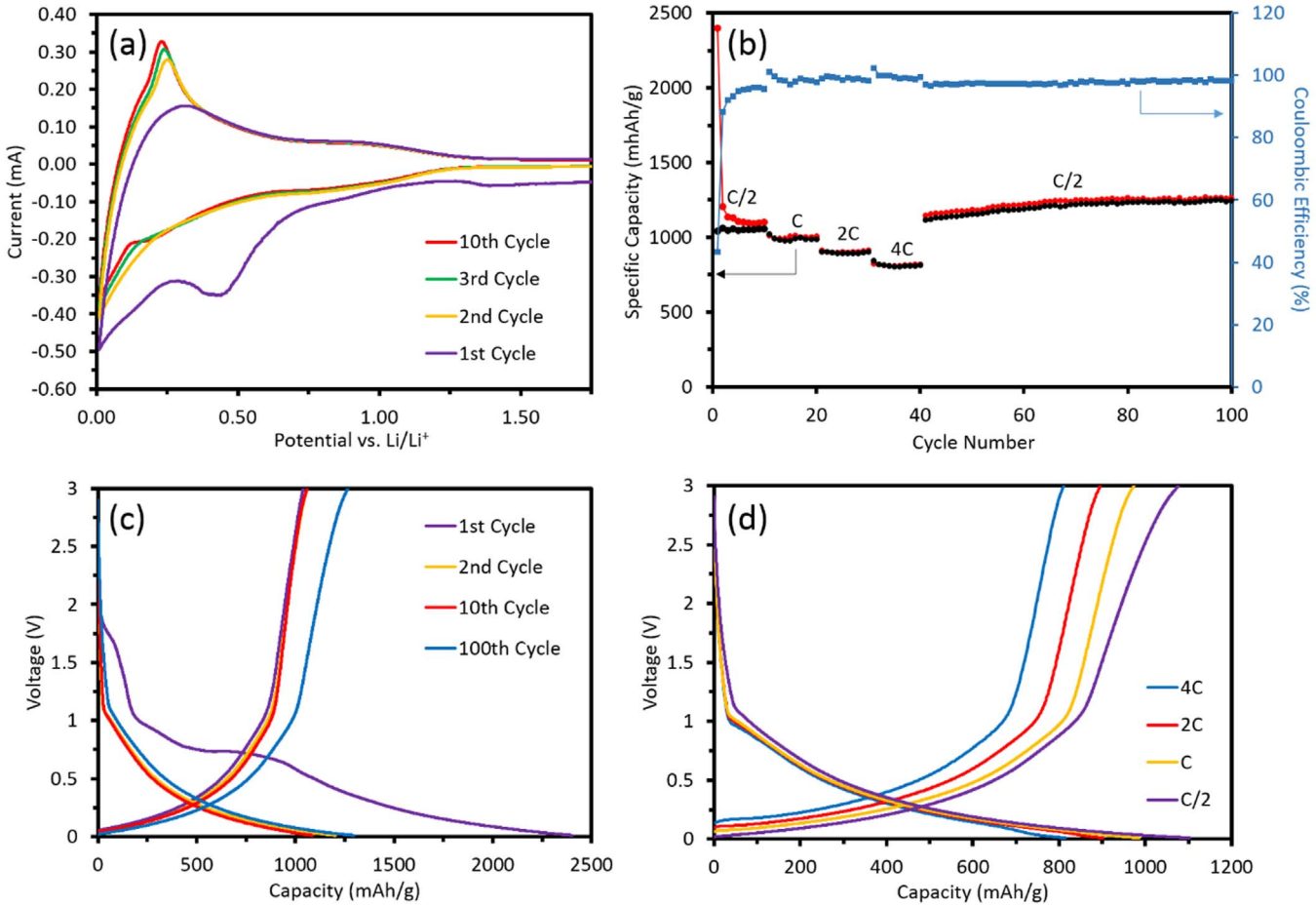

Figure 5 | (a) CV of SiO_2 NTs using a scan rate of 0.1 mVs^{-1}. (b) Charge-discharge capacities versus cycle number using a C rate of 100 mAg^{-1}. (c) Galvanostatic voltage profiles for SiO_2 NTs at a C/2 rate at selected cycles. (d) Galvanostatic voltage profiles for SiO_2 NTs at selected C rates.

et al. proposed capacity in SiO_2 anodes increases over time due to growth of the Si phase and, thus, a growth in Si volume. The formation of Li_ySiO_x at Si/SiO_x boundaries leads to the formation of three-fold coordinated Si [Si(III)] which reflects through SiO_4 tetrahedra to bond to the silicon phase. The capacity gained by inclusion of new Si atoms (~4 Li per Si) in the Si phase outweighs the loss in capacity due to the consumption of SiO_2 in the irreversible formation of Li_ySiO_x[54]. We do not attribute this increase in capacity to increases in operating environment temperatures as several cells were tested in a staggered sequence with the same phenomenon observed in all cells. CV also supports this claim via the significant heightening and narrowing of the dealloying peak, suggesting more Li^+ is able to be dealloyed from the SiO_2 NTs in subsequent cycles. The emergence of an anodic peak at 0.22 V in the CV plot by the 10^{th} cycle is consistent with the lithiation of Si.

Coin cells were disassembled after 100 galvanostatic charge-discharge cycles in an argon-filled glovebox. Electrodes were fully charged to remove reversibly alloyed lithium from the tubes. SiO_2 NT electrodes were rinsed with acetonitrile to remove electrolyte and then etched in 0.1 M HCl to remove the SEI layer and reveal post-cycling tube morphology. The SiO_2 NTs have undergone slight changes in morphology as evidenced in the TEM image in Fig. 6.

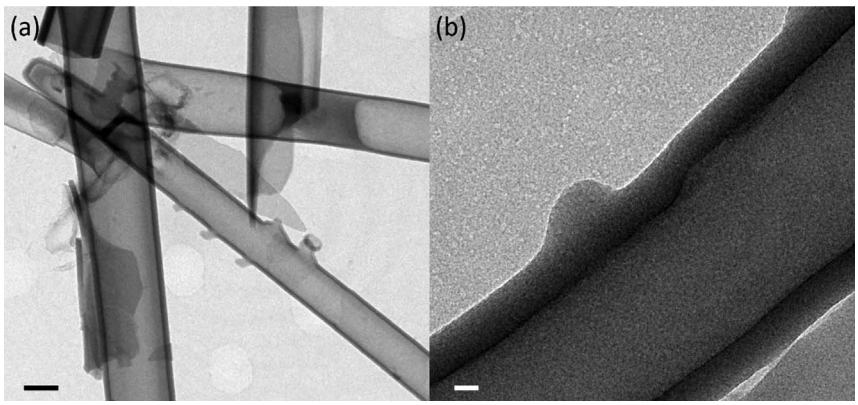

Figure 6 | (a) TEM image of an isolated SiO_2 NT after 100 galvanostatic charge-discharge cycles. (b) Higher magnification TEM image of the same SiO_2 NT emphasizing tube wall thickness and morphology. The scale bars are 200 nm and 20 nm for (a) and (b), respectively.

Cycled SiO_2 NTs still retain their tubular morphology but have developed slight undulations in the walls with variations in wall thickness. This preservation of the SiO_2 tube morphology post-cycling has also been confirmed by Wu et al. even after 2000 cycles[10].

In conclusion, SiO_2 NTs have been fabricated via facile two step templated process through thermal degradation of PDMS in air under vacuum. This environmentally friendly synthesis route uses abundant, non-toxic, and non-flammable precursors and yields SiO_2 NTs that produce a capacity of 1266 mAh g^{-1} after 100 cycles with minimal capacity fading. Galvanostatic cycling reveals a noticeable increase in capacity over the first 80 cycles, which is attributed to growth of a nano-Si phase upon generation of Li_ySiO_2 at Si/SiO_2 boundaries.

Methods

Synthesis of SiO_2 NTs were achieved via the following synthesis steps: Sylgard silicone elastomer was mixed in a 10 : 1 ratio with the curing agent and the mixture was set at 140°C for 10 minutes to form a solid PDMS block. The PDMS block was cut via straight-blade into 50 mg blocks and placed in a graphite crucible. Whatman Anodisc Anodic Aluminum Oxide templates with the following properties were used: 13 mm in diameter, 0.2 um pore diameter, and 50 μm template thickness. Six AAO templates were placed inside the crucible next to the PDMS block and placed inside a quartz tube in a MTI GSL1600X box furnace. The system was pumped down to 300 torr with a slow ambient air flow to allow for sufficient oxygen supply for the PDMS thermal degradation reaction. The system was heated to 650°C and held for 1 hour to allow for complete reaction of all PDMS. After cooling, templates were sonicated in IPA for 10 s to remove excess and loosely-bonded SiO_2 and dried under nitrogen stream. The SiO_2 coated AAO templates were placed in 50% wt H_3PO_4 and etched for 48 hours at 70°C to completely dissolve the AAO template. The SiO_2 NTs were washed several times with DI water and dried at 90°C under vacuum for 1 hour. SiO_2 NTs were then sonicated in IPA for 30 minutes to break apart the bundles of SiO_2 NTs and then dried under vacuum at 90°C for 1 hour.

Characterization. The morphology of the sample is studied via scanning electron microscopy (SEM, leo-supra, 1550) with an X-ray energy-dispersive spectroscopy (EDS). Transmission electron microscopy (TEM, Philips, CM300) with an acceleration voltage at 300 kV is used to perform the high resolution imaging. The TEM sample was prepared by dropping pre-dispersed SiO_2 NTs onto carbon film coated TEM grids.

Electrochemical Measurements. Electrochemical performance of SiO_2 NTs was characterized vs. Li using CR2032 coin cells with an electrolyte comprising 1 M $LiPF_6$ in ethylene carbonate and diethyl carbonate (EC:DEC = 1 : 1, v/v). Electrodes were prepared via mixing SiO_2 NT powder, Super P acetylene black, and polyvinyldene fluoride (PVdF) in a weight ratio of 5 : 3 : 2. The slurry was then compressed onto copper foils and allowed to dry at 90°C for 12 hours. Cells were assembled in an Argon-filled VAC Omni-lab glovebox. All cells were tested vs. Li from 0.01 to 3.0 V using an Arbin BT2000 at varying current densities. Cyclic voltammetry measurements were conducted on a Biologic VMP3 at a scan rate of 0.1 mVs^{-1}. The loading density of SiO_2 NTs on copper foils was 2.73 $mgcm^{-2}$.

1. Kasavajjula, U., Wang, C. & Appleby, J. A. nano- and bulk-silicon-based anodes for lithium-ion secondary cells. *J. Power Sources* **163**, 1003–1039 (2007).
2. Boukamp, B. A., Lesh, G. C. & Huggins, R. A. All-Solid Lithium Electrodes with Mixed-Conductor Matrix. *J. Electrochem. Soc.* **128**, 725–729, doi:10.1149/1.2127495 (1981).
3. Beaulieu, L. Y., Eberman, K. W., Turner, R. L., Krause, L. J. & Dahn, J. R. Colossal Reversible Volume Changes in Lithium Alloys. *Electrochem. Solid St.* **4**, A137–A140 (2001).
4. Song, T. *et al.* Arrays of Sealed Silicon Nanotubes As Anodes for Lithium Ion Batteries. *Nano Lett.* **10**, 1710–1716 (2010).
5. Liu, X. H. *et al.* Size-Dependent Fracture of Silicon Nanoparticles During Lithiation. *ACS Nano* **6**, 1522–1531 (2012).
6. Yao, Y. *et al.* Interconnected Silicon Hollow Nanospheres for Lithium-Ion Battery Anodes with Long Cycle Life. *Nano Lett.* **11**, 2949–2954 (2011).
7. Wu, H. *et al.* Stable Li-ion battery anodes by *in-situ* polymerization of conducting hydrogel to conformally coat silicon nanoparticles. *Nat. Comm.* **4**, (2012).
8. Yoo, J.-K., Kim, J., Jung, Y. S. & Kang, K. Scalable Fabrication of Silicon Nanotubes and their Application to Energy Storage. *Adv. Mater.* **24**, 5452–5456 (2012).
9. Chan, C. K. *et al.* High-performance lithium battery anodes using silicon nanowires. *Nat. Nanotechnol.* **3**, 31–35 (2007).
10. Wu, H. *et al.* Stable cycling of double-walled silicon nanotube battery anodes through solid-electrolyte interphase control. *Nat. Nanotechnol.* **7**, 310–315 (2012).
11. Ge, M., Rong, J., Fang, X. & Zhou, C. Porous Doped Silicon Nanowires for Lithium Ion Battery Anode with Long Cycle Life. *Nano Lett.* **12**, 2318–2323 (2012).
12. Liu, N. *et al.* A Yolk-Shell Design for Stabilized and Scalable Li-Ion Battery Anodes. *Nano Lett.* **12**, 3315–3321 (2012).
13. Kondo, S., Tokuhashi, K., Nagai, H., Iwasaka, M. & Kaise, M. Spontaneous ignition limits of silane and phosphine. *Combust. Flame* **101**, 170–174 (1995).
14. Guo, B. *et al.* Electrochemical reduction of nano-SiO_2 in hard carbon as anode material for lithium ion batteries. *Electrochem. Commun.* **10**, 1876–1878 (2008).
15. Yaroshevsky, A. A. Abundances of Chemical Elements in the Earth's Crust. *Geochem. Intl.* **44**, 48–55 (2006).
16. Miyachi, M., Yamamoto, H., Kawai, H., Ohta, T. & Shirakata, M. Analysis of SiO Anodes for Lithium-Ion Batteries. *J. Electrochem. Soc.* **152**, A2089–A2091 (2005).
17. Li, X. *et al.* Nanoporous tree-like SiO_2 films fabricated by sol-gel assisted electrostatic spray deposition. *Micropor. Mesopor. Mat.* **151**, 488–495 (2012).
18. Yao, Y., Zhang, J., Xue, L., Huang, T. & Yu, A. Carbon-coated SiO_2 nanoparticles as anode material for lithium ion batteries. *J. Power Sources* **196**, 10240–10243 (2011).
19. Yan, N. W., Fang Zhong, Hao Li, Yan Wang, Yu Hu, Lin Chen & Qian wang. Hollow Porous SiO2 Nanocubes Towards High-performance Anodes for Lithium-ion Batteries. *Sci. Rep.* **3** (2013).
20. Yang, J., Takeda, Y., Capiglia, C., Xie, J. Y. & Yamamoto, O. SiO_x-based anodes for secondary lithium batteries. *Solid State Ionics* **152–153**, 125–129 (2002).
21. Song, K. *et al.* Hierarchical SiO_x nanoconifers for Li-ion battery anodes with structural stability and kinetic enhancement. *J. Power Sources* **229**, 229–233 (2013).
22. Wang, J., Zhao, H., He, J., Wang, C. & Wang, J. Nano-sized SiO_x/C composite anode for lithium ion batteries. *J. Power Sources* **196**, 4811–4815 (2011).
23. Mao, O. *et al.* Active/Inactive Nanocomposites as Anodes for Li-Ion Batteries. *Electrochem. Solid St.* **2**, 3–5 (1999).
24. Xiang, H. F. *et al.* Graphene sheets as anode materials for Li-ion batteries: preparation, structure, electrochemical properties and mechanism for lithium storage. *RSC Adv.* **2**, 6792–6799 (2012).
25. Landi, B. J., Cress, C. D. & Raffaelle, R. P. High energy density lithium-ion batteries with carbon nanotube anodes. *J. Mater. Res.* **8**, 1636–1644 (2010).
26. Wang, W. *et al.* Pillared CNT and Graphene Nanostructure for Lithium Ion Battery Anode. *Nano Energy* (2013).
27. Wang, W., Guo, S., Ozkan, M. & Ozkan, C. S. Chrysanthemum like carbon nanofiber foam architectures for supercapacitors. *J. Mater. Res.* **28**, 912–917 (2013).
28. Wang, W. *et al.* Three dimensional few layer graphene and carbon nanotube foam architectures for high fidelity supercapacitors. *Nano Energy* **2**, 294–303 (2013).
29. Wang, W. *et al.* Intertwined Nanocarbon and Manganese Oxide Hybrid Foam for High-Energy Supercapacitors. *Small* (2013).
30. Wang, W. *et al.* Hybrid Low Resistance Ultracapacitor Electrodes Based on 1-Pyrenebutyric Acid Functionalized Centimeter-Scale Graphene Sheets. *J. Nanosci. Nanotechno.* **12**, 6913–6920 (2012).
31. Lian, P. *et al.* Large reversible capacity of high quality graphene sheets as an anode material for lithium-ion batteries. *Electrochim. Acta* **55**, 3909–3914 (2010).
32. Zhang, W.-M. *et al.* Tin-Nanoparticles Encapsulated in Elastic Hollow Carbon Spheres for High-Performance Anode Material in Lithium-Ion Batteries. *Adv. Mater.* **20**, 1160–1165 (2008).
33. Kim, J.-H., Khanal, S., Islam, M., Khatri, A. & Choi, D. Electrochemical characterization of vertical arrays of tin nanowires grown on silicon substrate as anode materials for lithium rechargeable microbatteries. *Electrochem. Commun.* **10**, 1688–1690 (2008).
34. AISBL, E. Linear Polydimethylsiloxanes. (European Centre for Ecotoxicology and Toxicology of Chemicals, Joint Assessment of Commodity Chemicals, 2011).
35. Graiver, D., Farminer, K. W. & Narayan, R. A Review of the Fate and Effects of Silicones in the Environment. *J. Polym. Environ.* **11**, 129–136 (2003).
36. Camino, G., Lomakin, S. M. & Lazzari, M. Polydimethylsiloxane Thermal Degredation Part 1. Kinetic Aspects. *Polymer* **42**, 2395–2402 (2001).
37. Camino, G., Lomakin, S. M. & Lageard, M. Thermal polydimethylsiloxane degradation. Part 2. The degradation mechanisms. *Polymer* **43**, 2011–2015 (2002).
38. Wang, Z., Zhou, L. & Lou, X. W. D. Metal Oxide Hollow Nanostructures for Lithium-ion Batteries. *Adv. Mater.* **24**, 1903–1911 (2012).
39. Wang, J., Du, N., Zhang, H., Yu, J. & Yang, D. Large-Scale Synthesis of SnO2 nanotube Arrays as High-Performance Anode Materials of Li-Ion Batteries. *J. Phys. Chem. C* **115**, 11302–11305 (2011).
40. Wu, H. *et al.* Engineering Empty Space between Si Nanoparticles for Lithium-Ion Battery Anodes. *Nano Lett.* **12**, 904–909 (2012).
41. Wang, B. *et al.* Contact-Engineered and Void-Involved Silicon/Carbon Nanohybrids as Lithium-Ion-Battery Anodes. *Adv. Mat.* **25**, 3560–3565 (2013).
42. Hu, Y., Ge, J. & Yin, Y. PDMS rubber as a single-source precursor for templated growth of silica nanotubes. *Chem. Comm.* 914–916, doi:10.1039/B820755K (2009).
43. Kasi, A. K., Kasi, K. J., Afzulpurkar, N., Hasan, M. M. & Mahaisavariya, B. Bending and branching of anodic aluminum oxide nanochannels and their applications. *J. Vac. Sci. Technol. B.* **30**, 031805–031807 (2012).
44. Obrovac, M. N. & Christensen, L. Structural Changes in Silicon Anodes during Lithium Insertion/Extraction. *Solid-State Lett.* **7**, A93–A96 (2004).
45. Wu, H. & Cui, Y. Designing nanostructured Si anodes for high energy lithium ion batteries. *Nano Today* **7**, 414–429 (2012).

46. Tee, J. C., Sanip, S. M., Aziz, M. & Ismail, A. F. Template Synthesis of Carbon Nanotubes. *AIP Conf. Proc.* **1217**, 217–221 (2009).
47. Nadimpalli, S. P. V. *et al.* Quantifying capacity loss due to solid-electrolyte-interphase layer formation on silicon negative electrodes in lithium-ion batteries. *J. Power Sources* **215**, 145–151 (2012).
48. Schroder, K. W., Celio, H., Webb, L. J. & Stevenson, K. J. Examining Solid Electrolyte Interphase Formation on Crystalline Silicon Electrodes: Influence of Electrochemical Preparation and Ambient Exposure Conditions. *J. Phys. Chem. C* **116**, 19737–19747 (2012).
49. Ren, Y. *et al.* Preparation and characterization of silicon monoxide/graphite/carbon nanotubes composite as anode for lithium-ion batteries. *J. Solid State Electr.* **16**, 1453–1460 (2012).
50. Jiang, T., Zhang, S., Lin, R., Liu, G. & Liu, W. Electrochemical Characterization of Cellular Si and Si/C Anodes for Lithium Ion Battery. *Int. J. Electrochem. Sc.* **8**, 9644–9651 (2013).
51. Kim, J.-H., Sohn, H.-J., Kim, H., Jeong, G. & Choi, W. Enhanced cycle performance of SiO-C composite for lithium-ion batteries. *J. Power Sources* **170**, 456–459 (2007).
52. Kim, T., Park, S. & Oh, S. M. Solid-State NMR and Electrochemical Dilatometry Study on Li^+ Uptake/Extraction Mechanism in SiO Electrode. *J. Electrochem. Soc.* **154**, A1112–A1117 (2007).
53. Chang, W.-S. *et al.* Quartz (SiO_2): a new energy storage anode material for Li-ion batteries. *Energy Environ. Sci.* **5**, 6895–6899 (2012).
54. Ban, C. *et al.* Lithiation of silica through partial reduction. *Appl. Phys. Lett.* **100**, (2012).

Author contributions

Z.F., W.W., M.O. and C.S.O. designed the experiments and wrote the main manuscript. Z.F., W.W., H.H.B. and A.G. worked on materials synthesis, battery fabrication, galvanostatic charge-discharge measurements, and testing at selected C rates. C.S.O. managed the research team. All authors reviewed the manuscript.

Additional information

Competing financial interests: The authors declare no competing financial interests.

How to cite this article: Favors, Z. *et al.* Stable Cycling of SiO_2 Nanotubes as High-Performance Anodes for Lithium-Ion Batteries. *Sci. Rep.* **4**, 4605; DOI:10.1038/srep04605 (2014).